ORIGINAL ARTICLE

LES validation of lock-exchange density currents interacting with an emergent bluff obstacle

M. Brito[1] · R. M. L. Ferreira[2] · A. Sousa[1] · R. Farias[1] · G. Di Lollo[3] · A. M. Ricardo[2] · L. Gil[1]

Abstract

We address the capability of large eddy simulation (LES) to predict the physics of density currents interacting with bluff obstacles. Most density currents of interest in engineering and geophysical applications interact with obstacles or topographic features. Validating LES solutions in these contexts is crucial to establish it as a trusted tool. We thus propose a validation effort based on simple geometries that nonetheless pose challenges common to more complex systems, including boundary layer separation and convective instabilities. We focus on lock-exchange gravity currents in the slumping phase interacting with an emergent vertical circular cylinder. Our main investment was in ensuring that the comparison of experimental data and numerical results include, at least, the velocity and the density fields , and derived quantities (e.g., second order moments). Measurements of both density and velocity fields were performed in the side and plan views for cylinder Reynolds numbers, Re_d, in the range 1300 to 3475. It was found that the LES accurately predicts the temporal evolution of the current front position. The computed front velocity exhibits a maximum relative error less than 8%. A good agreement between the LES and the experimental size and shape of the current head, and billows was found. The overall features upstream the cylinder, including a reflected wave, adverse pressure gradient and backflow, and downstream the cylinder, including the backflow, wake and the formation of a new head are well reproduced by LES. The agreement between the LES and the experimental time-space evolution of current spanwise- and depth-averaged density contours and the instantaneous velocity fields are not affected by Re_d.

Keywords Density currents · Bluff obstacles · Large eddy simulation (LES) · Flow-structure interaction

---

✉ M. Brito
moisesbrito@fct.unl.pt

1 UNIDEMI, Department of Mechanical and Industrial Engineering, Faculty of Science and Technology, Universidade Nova de Lisboa, 2829-516 Caparica, Portugal

2 CERIS, Instituto Superior Técnico, Universidade de Lisboa, Av. Rovisco Pais, 1049-001 Lisboa, Portugal

3 Department of Engineering, Roma Tre University, 00146 Rome, Italy

1 Introduction

The interaction between density currents and bluff obstacles is of practical importance for many engineering and geophysical applications, as pointed out by Simpson [37]. The prediction of this complex flow-structure interaction has been an active research area in recent years, using a wide variety of numerical modelling techniques, spanning the entire range from shallow water to high-resolution Navier-Stokes equations, including Reynolds-averaged Navier-Stokes (RANS) equations, large eddy simulation (LES), and direct numerical simulation (DNS). A review of the strengths and challenges of these techniques can be found in Meiburg et al. [27]. For currents with significantly high Reynolds number, LES is a good compromise between simulation detail, often insufficient in RANS, and computational cost, often prohibitive in DNS.

The potential of using LES in the modeling of Boussinesq currents at different Reynolds numbers in straight channels was reviewed by Constantinescu [11]. A significant progress has been made by several authors in the validation of density field characteristics. Ooi et al. [28] and Mahdinia et al. [25] have used available empirical data of classic unobstructed lock-exchange density currents in a straight channel of Hacker et al. [21]. The current front position and velocity during the slumping phase were well predicted in all simulations. However, the local size and shape of the main current features were qualitatively compared. Ottolenghi et al. [29] have also compared LES results with own experimental data of unobstructed lock-exchange density currents in a straight channel. A reasonable agreement was found with relative error less than 7%. This quantitative comparison was performed only between the numerical and the experimental current front positions. Recently, Zhou et al. [44] have used experimental data of Cenedese et al. [9] to compare LES density fields of two typical flow structures for a gravity current propagating past a bottom roughness. A good agreement between the LES and the experimental density fields was found. However, this qualitative comparison was made on a small window of the current head. Furthermore, in these studies, velocity field measurements were not used in the validation procedure.

Large eddy simulation of gravity currents interacting with array of bluff obstacles in flat bed have been studied by several authors e.g., Tokyay et al. [40, 41]; Ozan et al. [30]; Zhou et al. [44]; Bhaganagar & Pillalamarri [4]. In those studies the effects of the geometrical parameters describing the array of bluff obstacles on the structure of the lock-exchange flow, total drag force acting on the gravity current, front velocity, entrainment, mixing, and global energy budget have been analysed and discussed. However, to better provide physical insights into these interactions, these complex configurations must be simple enough to allow for sound interpretations but must possess elements with the same complexity of the real-life applications, albeit in schematic form such as an isolated bluff obstacle [13, 18]. Large eddy simulation modelling of the structure of density currents interacting with an isolated obstacle mounted on a flat bed surface or situated at a small distance from the flat bed have been performed by Gonzalez-Juez et al. [18–20]. These studies provided quantitative insight into the physical mechanisms generating the drag forces on the obstacle during the different stages of the interaction between density currents and the bluff obstacle. Large eddy simulation provided detailed information on the evolution of the flow upstream (e.g., speed of the reflected jump, depth of the reflected flow) and downstream of the obstacle (e.g., front velocity, head height, fraction of the flow convected over the obstacle). The temporal variation of the drag and lift forces induced by gravity currents impacting circular and square cylinders separated by a gap from the bottom wall were compared with experimental data of Ermanyuk & Gavrilov [13, 14]. Such studies not specifically addressed

at validating the numerical tool. Furthermore, in the literature, there are no studies with comparison of both velocities and density fields in controlled situations. We address this research gap.

This paper provides a validation of 3D-LES of lock-exchange density currents interacting with an emergent circular cylinder in the slumping phase. The validation is performed by comparing LES results with a new experimental results of both density and velocity fields. Measurements were performed in both side and plan views for Re_d ranging from 1300 to 3475. The experimental set-up, instrumentation, data collection and processing methods are described in Sect. 2. The numerical approach, LES technique, computational domain, boundary conditions and numerical parameters are presented in the Sect. 3. In order to assess the reliability of the LES technique to predict lock-exchange density currents interacting with an emergent circular cylinder, LES solutions of the kinematics of the current front, spanwise-averaged current density field, depth-averaged current structure, and velocity vector fields are compared with experimental results in Sect. 4. The main findings are summarized in Sect. 5.

2 Laboratory experiments

2.1 Experimental setup

For LES model validation, a series of laboratory tests were conducted in a flat and rectangular cross-section channel at the DEMI laboratory of Faculty of Science and Technology, Universidade Nova de Lisboa, Portugal. The schematic diagram (not to scale) of the experimental set-up is shown in Fig. 1. It should be noted that x^*, y^* and z^* are dimensionless Cartesian coordinates scaled using the initial fluid depth in the lock, $h_0 = 0.2$ m. The channel is $15h_0$ long, $0.875h_0$ wide and $2h_0$ deep. The gravity current was generated using the classic lock-exchange configuration. A sliding stainless steel gate with 1 mm thickness
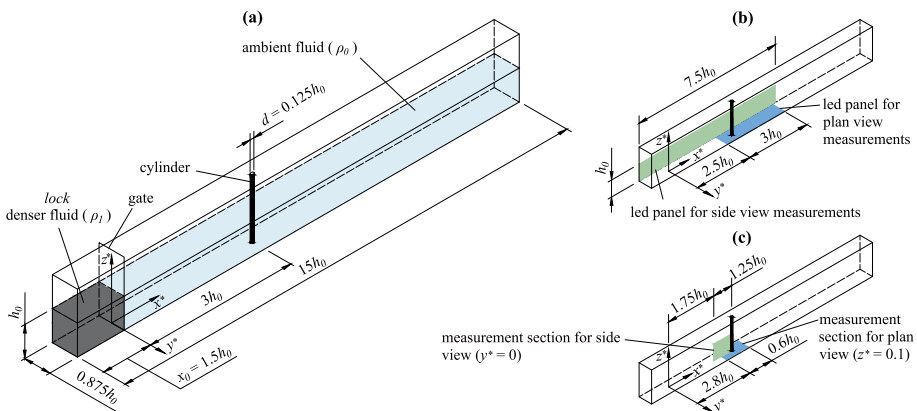
Fig. 1 Schematic of the experimental set-up (not to scale) showing the **a** main dimensions and the Cartesian reference system, **b** illuminated section for side view ($h_0 \times 7.5h_0$) and plan view ($0.875h_0 \times 3h_0$) of density field measurements, and **c** measurement section for side view ($1.25h_0 \times h_0$) and plan view ($0.6h_0 \times 0.4h_0$) of velocity field measurements. All dimensions are scaled using initial water depth, h_0

was positioned at $x^* = 0$, forming a lock with the length $x_0 = 1.5h_0$ from the left hand side of the channel (upstream section in Fig. 1a).

The emergent vertical cylinder was positioned in the centre line of the channel ($y^* = 0$) in the ambient fluid region at $3h_0$ downstream of the gate (Fig. 1a). The cylinder is made of PVC with a diameter $d = 0.125h_0$.

In all experiments, both lock and ambient regions were filled up to the same depth, h_0. In the gap between channel walls and gate, a film of vaseline was used to prevent leakage. The denser fluid with initial density ρ_1 was a mixture of fresh water, salt and Rhodamine WT Liquid with specific density of 1.15 at 20 °C. The ambient fluid with density ρ_0 was a solution of clear denatured ethanol and fresh water. This ethanol-water mixture was introduced to match the refractive index of the denser fluid, enabling accurate results with optical measurement techniques. The amount of salt and alcohol was calculated by a procedure similar to that proposed by Daviero et al. [12]. Both solutions were mixed vigorously for about 10 min to assure that the denser and ambient fluids were homogeneous before the experiment was initiated [10]. As the density difference between fluids is a result of both temperature and concentration, these parameters were measured in the beginning of each run for both fluids. The density was measured using a 100 ml pycnometer with a precision of 0.001 ml. The temperature was measured using a thermometer with a precision of 0.1 ° C.

2.2 Instrumentation

Both density and velocity fields were measured in the x–z plane (plan view) and in the x–y plane (side view) at specific locations (Fig. 1b and c).

The density fields were obtained using a light attenuation technique from backlight. The raw images were recorded using an Allied Vision Bonito CL-400B/C high-speed camera with a resolution of 1024×254 pix^2 at a framerate of 50 Hz. In order to acquire density using light attenuation technique, the flow was illuminated by a white led panel with 48 W, 3680 LM and 6500 K from the rear and from the under in side and plan layouts, respectively (Fig. 1b). In the side view, the field of view of the camera was a rectangular cross-section with $h_0 \times 7.5h_0$. In the plan view, it was a rectangular cross-section with $0.875h_0 \times 3h_0$ (Fig. 1b).

Two components of the velocity fields in the side view, u and w, and in plan view, u and v, were measured with a 2D particle image velocimetry (PIV) system. It consists of a double-cavity neodymium-doped yttrium aluminum garnet (Nd:YAG) laser source able to generate a pulse of 30 mJ. The output laser beam is green with wavelength of 532 nm. This system is described in Ferreira [16]; Ricardo et al. [34]; Brito et al. [7]. A charged coupled device (CCD) Flowsense 2M camera, commercialized by Dantec, with a resolution of 1600×1200 pix^2 was positioned perpendicularly to the laser sheet in both layouts. The PIV system was operated with a maximum sample frequency of 15 Hz and a time between two consecutive laser pulses of 500 μs. The synchronization between the PIV system and gate was performed using an external trigger connected to the gate and PIV timer box [7]. Polyamid particles with nominal diameter of 50 μm and specific density of 1.03 were used as tracer particles. The measurement section in the side view is located at the middle of channel ($y^* = 0$) and upstream of the cylinder with a rectangular cross-section of $1.25h_0 \times h_0$. In the plan view it is located at $z^* = 0.1$ with a cross-section of $0.6h_0 \times 0.4h_0$ (Fig. 1c).

The calibration of both measurement techniques are described in Sect. 2.4.

2.3 Experimental tests

The laboratory experiments were carried out for four values of the reduced gravity $g_0' = g(\rho_1 - \rho_0)/\rho_0$ as presented in Table 1. Measurements were taken in both side (S) and plan views (P). The main parameters for all tests are listed in Table 1, where U_f^* is the dimensionless time-averaged gravity current front velocity scaled by the initial buoyancy velocity, $U_0 = \sqrt{g_0' h_0}$. In this paper, U_f is calculated as the time derivative of the front position [35, 44]. The flow parameters $Re_0 = U_0 h_0/\nu$ is the channel Reynolds number, ν is kinematic viscosity of ambient fluid, $Re_d = U_f d/\nu$ is the cylinder Reynolds number and $Fr_0 = U_f/\sqrt{g_0' h_0}$ is the total depth densimetric Froude number. The initial density ratio is defined as $\gamma_0 = \rho_0/\rho_1$.

Each test in Table 1 represents 10 runs, each with identical initial conditions. Each run starts when the gate is suddenly removed, leaving the denser fluid to flow along the bottom of the channel, while the ambient fluid (lighter fluid) moves above in the opposite direction.

2.4 Data processing

The data were analysed using in-house Matlab and Python scripts, following an approach similar to Hacker et al. [21]; Fragoso et al. [17]; van Sommeren et al. [43]; Sher & Woods [36]; Bardoel et al. [2] for density field measurements and similar to Ricardo et al. [34]; Brito et al. [7] for velocity field measurements.

The conversion of grey scale into density field of each recorded image was based on the attenuation of the light passing through the fluid column, i.e., the light absorbed along the path from the back to the front wall of the channel in the side view measurements, and from bottom wall to the free-surface in the plan view measurements. The amount of salt and Rhodamine present in the water promote this light attenuation that can be used to assess spanwise- and depth-averaged density distribution in the side and plan view measurements, respectively. This approach requires a pixel-by-pixel calibration procedure.

In this paper, the calibration procedure was carried out by successive removal of denser fluid (a mixture of fresh water, salt and Rhodamine) and addition of ambient fluid (a solution of clear denatured ethanol and fresh water) through the channel [39]. As the grey scale values show a non-linear variation with density, 32 frames after subsequent dilution were considered. The corresponding images were captured with the same light conditions and camera position. The first frame was obtained filling the channel with denser fluid (ρ_1). The 30 subsequent frames were obtained remove denser fluid and add ambient fluid. The last frame was obtained filling the channel with ambient fluid (ρ_0). A linear interpolation was applied to each pixel in the calibration curve to convert the grey scale values at any given pixel of each recorded image into density. To avoid the spatial oscillations on the density

Table 1 Main parameters of the experiments for the side view (S) and plan view (P)

Test	g_0' (m s^{-2})	U_f^*	γ_0	Re_0	Re_d	Fr_0
S1, P1	0.06	0.473	0.994	22,000	1300	0.475
S2, P2	0.12	0.471	0.988	31,000	1825	0.471
S3, P3	0.24	0.457	0.976	43,800	2500	0.456
S4, P4	0.48	0.448	0.953	62,000	3475	0.449

field a median of $3 \times 3 \text{ pix}^2$ was used in the calibration procedure [15]. A metric scale was used to convert from units of pixels to metric values.

The PIV data processing was firstly carried out in the DynamicStudio software. The raw images in the side view tests were interrogated in an area of $16 \times 16 \text{ pix}^2$ and in the plan view in $32 \times 32 \text{ pix}^2$. In both tests a 50% overlap and an adaptive (multi-pass with deformable and decreasing windows) correlation algorithm were used [24]. Vector validation was based on the local median of the eight neighbouring vectors. The instantaneous velocity datasets computed in DynamicStudio were exported to scripts for further analysis. The data were converted to metric units using a rectangular glass plates with a square mesh grid of $5 \times 5 \text{ mm}^2$ to convert units of pixels to metric values. Further details of the data processing can be found in Lollo [24]; Ramos [33].

3 Description of numerical approach

The OpenFOAM implementation of LES model was used to simulate the lock-exchange density currents interacting with an emergent circular cylinder. The current can be classified as a Boussinesq's density current as the density ratio $\gamma_0 = \rho_0/\rho_1 \sim 1$ [6]. Under this fundamental hypothesis, the governing equations (filtered continuity, Navier-Stokes and solute mass conservation equations for 3D unsteady and incompressible stratified flows), written with Einstein summation notation and in dimensionless form, are

$$\frac{\partial \overline{u_i^*}}{\partial x_i^*} = 0 \tag{1}$$

$$\frac{\partial \overline{u_i^*}}{\partial t^*} + \frac{\partial \overline{u_i^* u_j^*}}{\partial x_j^*} = -\frac{\partial \overline{p^*}}{\partial x_i^*} + \frac{\partial}{\partial x_j^*}\left(\frac{1}{Re_0}\frac{\partial \overline{u_i^*}}{\partial x_j^*}\right) - \frac{\partial \tau_{ij}^*}{\partial x_j^*} + \overline{\rho^*}e_i^g \tag{2}$$

$$\frac{\partial \overline{\rho^*}}{\partial t^*} + \frac{\partial \overline{\rho^* u_j^*}}{\partial x_j^*} = \frac{\partial}{\partial x_j^*}\left(\frac{1}{Sc\,Re_0}\frac{\partial \overline{\rho^*}}{\partial x_j^*}\right) - \frac{\partial \tau_j^{*\rho}}{\partial x_j^*} \tag{3}$$

where the asterisk denotes a dimensionless variable and the overbar stands for a filtered flow variable. The dimensional variables are the Cartesian coordinates x_i and velocity components u_i in i-direction, time t, pressure p and fluid density ρ. The Einstein notation for summation is employed and $x \equiv x_1$, $y \equiv x_2$ and $z \equiv x_3$ (Fig. 1). The flow velocity components are also denoted as $u \equiv u_1$ (streamwise), $v \equiv u_2$ (spanwise) and $w \equiv u_3$ (vertical). The characteristic length and velocity scales are the initial current height h_0 and the initial buoyancy velocity $U_0 = \sqrt{g(\rho_1 - \rho_0)h_0/\rho_0}$ where ρ_1 and ρ_0 are the density of denser and ambient fluids, respectively. The dimensionless variables are defined as $x_i^* = x_i/h_0$, $u_i^* = u_i/U_0$, $\rho^* = (\rho - \rho_0)/(\rho_1 - \rho_0)$, $p^* = p/(\rho_0 U_0^2)$ and $t^* = tU_0/h_0$. Here, e_i^g is the normalized gravity acceleration vector defined as $g_i/|g_i|$. The flow parameters are the channel Reynolds number $Re_0 = U_0 h_0/\nu$ and the Schmidt number $Sc = \nu/\mathcal{D}$, where $\mathcal{D}$ is the molecular diffusivity coefficient. The unknown terms $\tau_{ij}^* = \overline{u_i^* u_j^*} - \overline{u_i^*}\,\overline{u_j^*}$ and $\tau_j^{*\rho} = \overline{\rho^* u_j^*} - \overline{\rho^*}\,\overline{u_j^*}$ are the subgrid-scale (SGS) momentum and mass flux tensors, respectively. The τ_{ij}^* is modeled using the Smagorinsky model [38] as

$$\tau_{ij}^* - \frac{1}{3}\delta_{ij}\tau_{kk}^* = -2\nu_{SGS}\overline{S_{ij}^*} \tag{4}$$

where δ_{ij} is the Kronecker delta and $\overline{S_{ij}^*}$ is the dimensionless resolved strain-rate tensor defined by

$$\overline{S_{ij}^*} = 2\left(\frac{\partial \overline{u_i^*}}{\partial x_j^*} + \frac{\partial \overline{u_j^*}}{\partial x_i^*}\right) \tag{5}$$

The SGS eddy viscosity ν_{SGS} is modeled as followed

$$\nu_{SGS} = \left(C_s\Delta\right)^2\sqrt{2\overline{S_{ij}^*}\,\overline{S_{ij}^*}} \tag{6}$$

where $\Delta = \left(\Delta_1\Delta_2\Delta_3\right)^{(1/3)}$ is the SGS filter scale which corresponds to the local grid size and C_s is the Smagorinsky constant, which depends on the flow, and different values have been proposed in the literature, here $C_s = 0.18$ was used [31]. The $\tau_j^{*\rho}$ is modeled in a similar manner, using an eddy diffusivity model as

$$\tau_j^{*\rho} = -\frac{\nu_{SGS}}{Sc_{SGS}}\frac{\partial \overline{\rho^*}}{\partial x_j^*} \tag{7}$$

where Sc_{SGS} is the the SGS Schmidt number. As in most of LES studies of turbulent density currents [28, 44] we employed $Sc_{SGS} = 1$. Convective and diffusive terms of the filtered governing Equations (2) and (3) are handled with a unbounded Gauss linear scheme and scalar transport is calculated using a Gauss-Van Leer scheme [4, 42, 44]. A second-order backward implicit method has been used for the temporal discretization [25]. The geometric agglomerated algebraic multiGrid (GAMG) preconditioner is used for solving the Poisson equation for pressure. The pressure-implicit with splitting of operators (PISO) algorithm is used to solve velocity-pressure fields [4, 23, 25]. This algorithm involves a predictor step followed by two corrector steps, i.e., the pressure correction equation is solved twice to ensure that the continuity equation is satisfied.

The 3D computational domain, aimed at realistically mimicking the experimental channel, is $L_x \times L_y \times L_z = 15h_0 \times 0.875h_0 \times h_0$, where L_x, L_y and L_z are the streamwise, spanwise and vertical directions, respectively. The density current is generated using the lock-exchange configuration where the computational domain is filled with denser fluid ρ_1 for $x^* < 0$ (with a volume of $1.5h_0 \times 0.875h_0 \times h_0$) while $x^* > 0$ contains ambient fluid (lighter fluid) ρ_0.

No-slip boundary conditions are imposed at the cylinder surface and at the bottom and lateral walls. For the accurate results, all boundary layers are explicitly resolved. In this context, the mesh is stretched in the normal direction near the cylinder, bottom and lateral walls with normal dimensionless distance $n^+ = \Delta n\, u_\tau/\nu < 2$, where Δn is the normal distance of the first mesh element from the walls and u_τ is the friction velocity. To achieve adequate boundary-layer resolution, about 20 cells are imposed within the layer $0 < n^+ < 100$, being 10 cells within the viscosity-affected near-wall region $n^+ < 10$ [31]. On the top wall, a shear-free boundary condition is applied. No-flux conditions are also enforced on all boundaries (wall-normal velocity is zero).

To discretize the domain, an extensive mesh sensitivity analysis was conducted to confirm the validity of the solver and the spatial and time resolutions, considering

$N_x \in \{500; 2500\}$ mesh points in streamwise, $N_y \in \{75; 250\}$ spanwise and $N_z \in \{75; 250\}$ vertical directions. As suggested in Pereira et al. [32], the mesh sensitivity analysis was conducted before validation. The time evolution of the dimensionless position of the current front $x_f^* = x_f/h_0$ of four different resolutions with total number of cells $N_x \times N_y \times N_z$ $= 500 \times 75 \times 75$, $1000 \times 100 \times 100$, $2000 \times 150 \times 200$ and $2500 \times 200 \times 200$ for tests S1 and S3 (Table 1) are presented in Fig. 2. As expected, the coarser resolution leads the largest average relative difference from finer resolution, about 25%. The mesh refinement reduces numerical uncertainties and for the two finer resolutions $2000 \times 150 \times 200$ and $2500 \times 200 \times 200$, the position of the current front exhibits small variations. The average relative difference between values corresponding to the two finer resolutions does not exceed 2%.

Based on this mesh sensitivity analysis, all the simulations in Sect. 4 are conducted using the mesh with the base size of $N_x \times N_y \times N_z = 2000 \times 150 \times 200$, which allows a good compromise between simulation detail and computational cost. The time step with an average value of $0.002 U_0/h_0$ was automatically adjusted by the solver to be as large as possible without affecting flow simulation accuracy and exceeding the stability limit giving by a maximum CFL (Courant–Friedrichs–Lewy) number of 0.5.

4 LES results and comparison with the experiments

4.1 Kinematics of the current front

The LES and experimental time evolution of the dimensionless position of the current front $x_f^* = x_f/h_0$ for tests S1 and S3 (Table 1) are compared in Fig. 3. Both LES and experimental x_f are calculated at each time instant using the inflection point of the spanwise-averaged dimensionless concentration field $\rho^*(x^*, y_A^*, z^*, t^*)$ with threshold value $\rho^* = 0.5$, the same as in Gonzalez-Juez et al. [18–20]. It should be noted that the A-subscript in the y^* direction denotes the averaging of density field in that direction, i.e. $\langle \rho^* \rangle_y(x^*, z^*, t^*) \equiv \rho^*(x^*, y_A^*, z^*, t^*)$. The inflection point of $\rho^*(x^*, y_A^*, z^*, t^*)$ in the head nose occurs closer to the bottom wall for $z^* \sim 0.1h^*$, where $h^* = h/h_0$ is the normalized density current height.
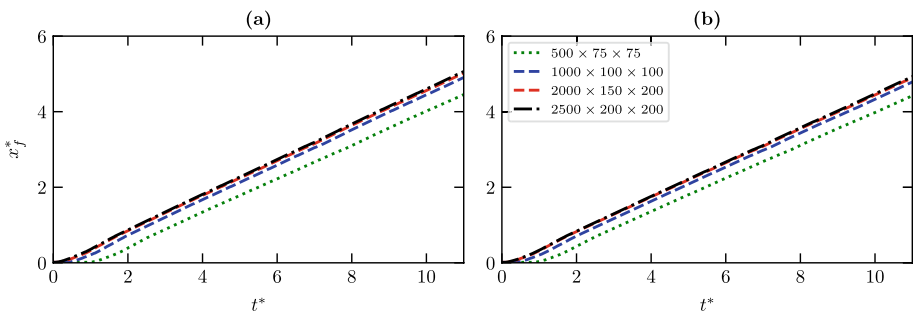

Fig. 2 Temporal evolution of dimensionless position of the current front x_f^* of four different meshes with total number of cells $N_x \times N_y \times N_z = 500 \times 75 \times 75$, $1000 \times 100 \times 100$, $2000 \times 150 \times 200$ and $2500 \times 200 \times 200$ for tests **a** S1 and **b** S3
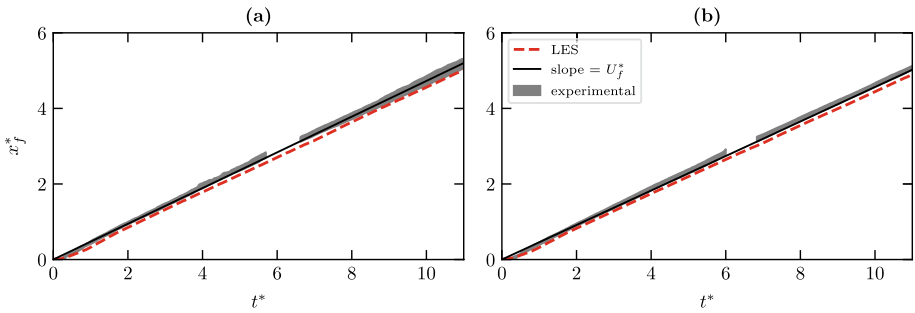
Fig. 3 Comparison of LES (dashed red line) and experimental (shaded region for the 10 runs) dimensionless position of the current front x_f^* as a function of dimensionless time t^* for tests **a** S1 and **b** S3. The shaded region corresponds to the standard deviation of each test. The solid back line shows analytical trend of x_f^* as a function of t^* with constant slope of U_f^* [37]

After a short initial acceleration phase ($t^* \lesssim 2$), the gravity current reaches the well-defined slumping phase ($t^* > 2$, extending until the end of the density field measurements $x^* = 5$ at $t^* \approx 11$) with a constant time-average front velocity, U_f, resulting in $x_f \propto t$ [22, 37]. It is observed that the effect of the cylinder on the evolution of bulk current front is not significant in both tests S1 and S3 (Fig. 3), contrarily what is seen in submerged isolated cylinders in which the current slows down [13, 18]. During the impact stage, the cylinder has effects on the current local features (see, Sects. 4.2–4.4). The time-averaged velocity U_f^* remains constant, i.e., the slope of temporal evolution of the current front position is approximately constant (Fig. 3). Figure 4 shows the spatial evolution of the dimensionless velocity of the current front u_f^* for tests S1 and S3. The noise in u_f^* was filtered by moving average. Tests S2 and S4 (not shown) also demonstrated similar temporal evolution of u_f^*. All LES results seem in a good agreement with experimental data, with the LES model predicting slightly larger initial acceleration. Similar trend has also been found by e.g., Mahdinia et al. [25] and Ozan et al. [30]. This initial acceleration phase is very difficult to spot in the plots showing the progression of the front location, see e.g., Cantero et al. [8]. This acceleration phase can be seen in Fig. 4, which depicts the spatial distribution of the front velocity. It is clear that the LES results feature an acceleration phase. However, this phase is not observed in the experimental results. Similarly, most experimental studies do
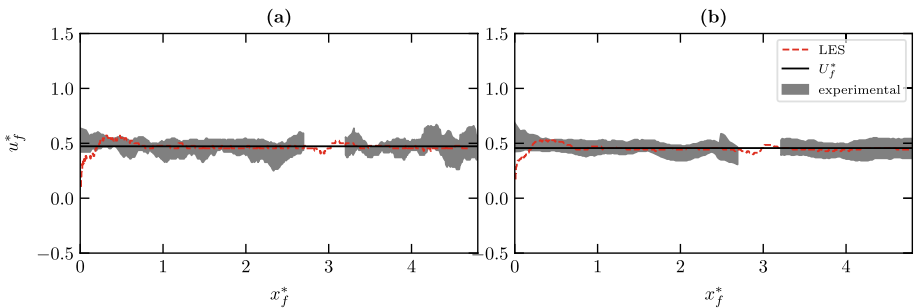
Fig. 4 Comparison of LES (dashed red line) and experimental (shaded region for the 10 runs) dimensionless velocity of the current front u_f^* as a function of x_f^* for tests **a** S1 and **b** S3. The shaded region corresponds to the standard deviation of each test. The solid back line is the dimensionless time-averaged gravity current front velocity U_f^*

not report a well-developed acceleration phase (e.g., Mariono et al. [26]; Adduce et al. [1]; Sher & Woods [36]). We can only speculate that the difference is the lock release mechanism. In the numerical case, it is the instantaneous elimination of a restriction to motion. The flow accelerates as the resultant of pressure forces slowly overcome viscous drag. In the case of the experimental tests, the lifting of the gate generates an updraft that is likely to generate a pressure drop that may increase the pressure imbalance by orders of magnitude. The flow would suffer a greater acceleration (beyond detection by the sample rate measurements) as viscous drag would be negligible relatively to the generated pressure imbalance.

For a more quantitative comparison, the agreement between LES and experimental results is quantified considering the mean and maximum of average relative error, defined as

$$\mathcal{E}_\psi = \frac{1}{10} \sum_{i=1}^{10} \left| \frac{\psi_i^{exp} - \psi^{num}}{\psi_i^{exp}} \right| \times 100 \tag{8}$$

where the superscripts *num* and *exp* refer to results of the LES and experimental runs of a ψ variable, respectively. The standard deviations associated with the measured quantities of the current front features are less than 5% for all tests. The maximum relative errors of position of the current front $\mathcal{E}_{x_f}$, front velocity $\mathcal{E}_{u_f}$, Froude number $\mathcal{E}_{Fr}$ and Reynolds number $\mathcal{E}_{Re}$ of the current defined, respectively, as $Re = u_f h/\nu$ and $Fr = u_f/\sqrt{g_0' h}$ for all side view tests are reported in Table 2. The instantaneous depth of the current, h, is defined using similar approach as presented in Bhaganagar & Pillalamarri [4].

Table 2 shows that LES can predict the kinematics of the current front with maximum relative error less than 8%. This relative error decreases with increasing g_0'. This may be caused by the finite time to remove the gate, as proposed by Ooi et al. [28]. For lower g_0', this upward gate removal in the experimental tests causes the lower layers to spread much more before the other layers are allowed to move [28]. The disturbance of the passing of the gate through the upper surface is also responsible for this problem, mainly for lower g_0'. The mixing speed for higher g_0' (larger current inertial forces) causes a small effect on the bulk features.

4.2 Spanwise-averaged current density field

The spanwise-averaged contours of the dimensionless concentration $\rho^*(x^*, y_A^*, z^*, t^*)$ at four different $t^* = 5, 6.5, 8$ and 10.5 for tests S1 and S3 are shown in Figs. 5 and 6, respectively. Both single experimental run and ensemble-averaged of the 10 runs are compared, as the unsteady billows, lobes and clefts in different runs are mismatched and smoothed by the ensemble-averaged (see the bottom contours in Figs. 5 and 6). Before the impact of the

Table 2 Maximum relative error of position of the current front $\mathcal{E}_{x_f}$, front velocity $\mathcal{E}_{uf}$, Froude number $\mathcal{E}_{Fr}$ and Reynolds number $\mathcal{E}_{Re}$

| Test	$\mathcal{E}_{x_f}$ (%)	$\mathcal{E}_{u_f}$ (%)	$\mathcal{E}_{Fr}$ (%)	$\mathcal{E}_{Re}$ (%)
S1	6.6	7.1	7.4	7.9
S2	4.9	5.8	6.1	6.3
S3	3.1	4.4	5.0	5.1
S4	0.8	2.7	3.3	3.8
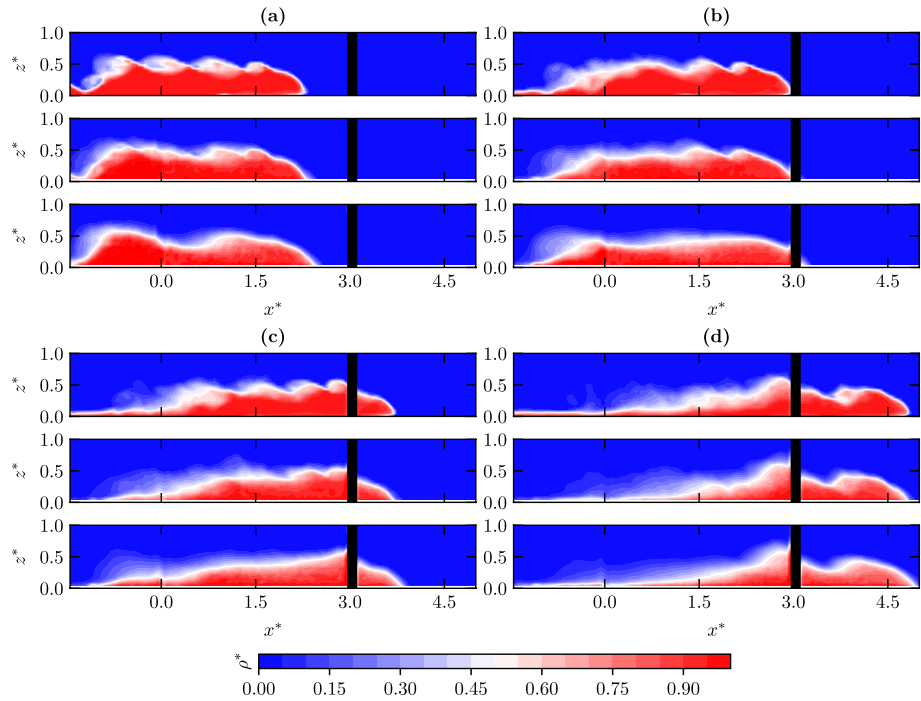
Fig. 5 LES (top), experimental single run (middle) and ensemble-averaged of the 10 experimental runs (bottom) of instantaneous spanwise-averaged dimensionless concentration contours $\rho^*(x^*, y_A^*, z^*)$ for test S1 at different dimensionless time **a** $t^* = 5$, **b** $t^* = 6.5$, **c** $t^* = 8$, and **d** $t^* = 10.5$

current on the cylinder, a similar distribution of ρ^* can be observed at $t^* = 5$ in both tests S1 and S3. The shape of the current head, billows, lobes and clefts at the interface of the two fluids are well predicted. However, close to the gate region at $x^* \approx 0$ there are some discrepancies, mainly in the tail of the current, attributed to the different boundary conditions on the gate, including vaseline used in the experiments to prevent leakage. As the tail drops, a plunging flow is observed in the ensemble-averaged of the 10 experimental runs. This plunging seems to increase with g_0' (see the bottom contours in Figs. 5a and 6a). Similar trend has also been found by Hacker et al. [21]. For the initial moment of impact of the current on the cylinder, at $t^* \approx 6.5$, the LES head nose is slightly higher than the experimental, with a relative error of about 5%. However, the shape of the head remains approximately the same as the current advances. At $t^* = 8$, the rear of the head is strongly modified by the cylinder with a surging of the current upstream of the cylinder $2.5 \lesssim x^* \lesssim 3$. This obstacle-induced can be also confirmed by the depth-averaged current structure analysis in Sect. 4.3 with increasing of depth-average density. This current surging upstream of the cylinder and the strong unsteady 3D structure of the flow cause the plunging downstream $3 \lesssim x^* \lesssim 3.5$ after the head has passed the cylinder at $t^* = 10$. The current head reestablishes downstream of the cylinder without changing the bulk velocity of the current front. At this instant the effect of the gate on the current tail becomes negligible and the overall shape of the concentration contours are also quite similar. This trend can be also observed in Figures 7, 8, 9, 10, 11 and 12. Together, the position of the diffuse wake ($x^* \approx 3.75$) is well predicted by LES.
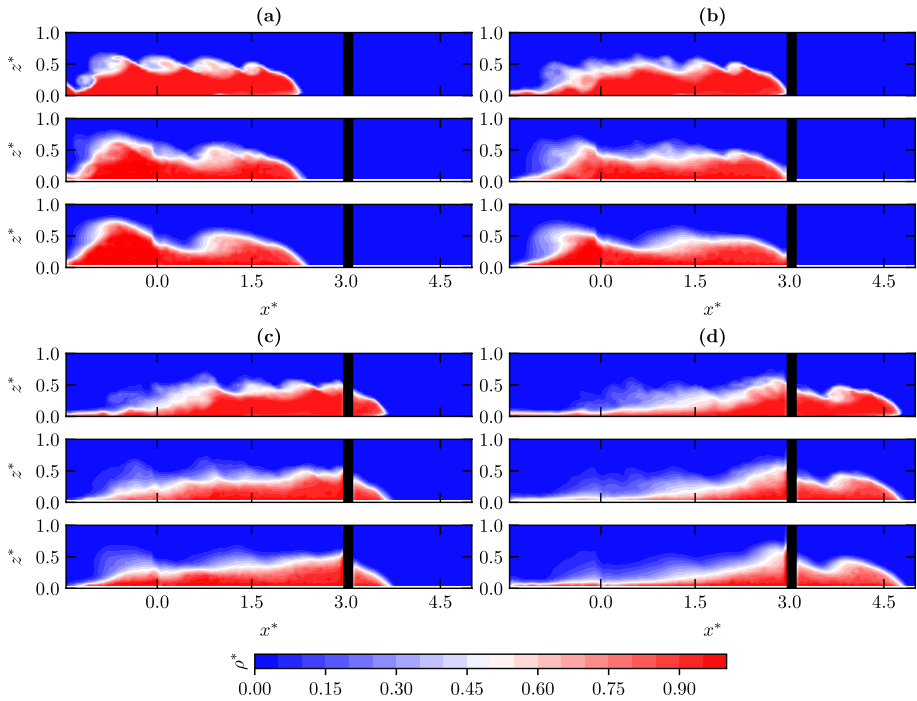
Fig. 6 LES (top), experimental single run (middle) and ensemble-averaged of the 10 experimental runs (bottom) of instantaneous spanwise-averaged dimensionless concentration contours $\rho^*(x^*, y_A^*, z^*)$ for test S3 at dimensionless time **a** $t^* = 5$, **b** $t^* = 6.5$, **c** $t^* = 8$, and **d** $t^* = 10.5$
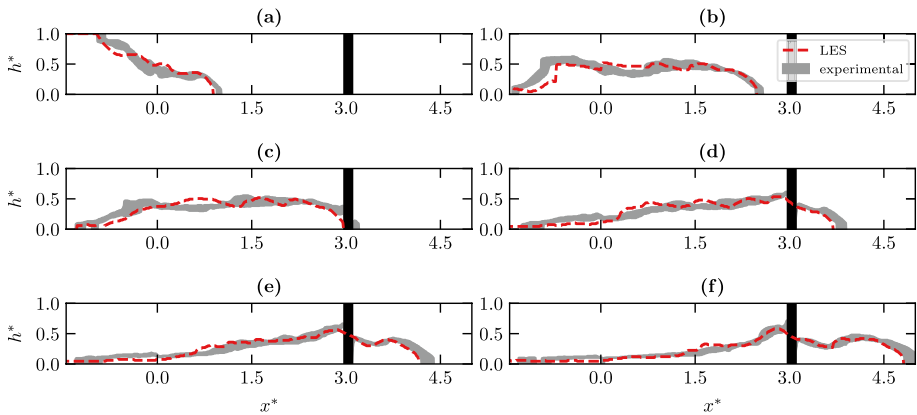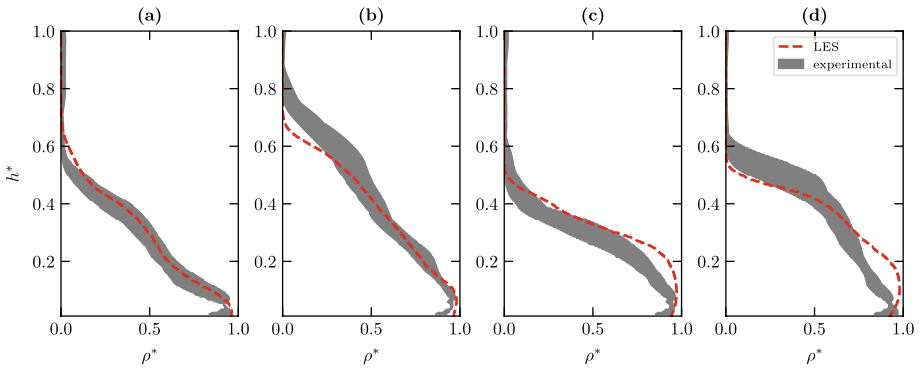

Fig. 7 LES (dashed red line) and experimental (shaded region) profiles of dimensionless current height h^* as a function of x^* for test S1 at **a** $t^* = 2$, **b** $t^* = 5$, **c** $t^* = 6.5$, **d** $t^* = 8$, **e** $t^* = 9$, and **f** $t^* = 10.5$

For a more quantitative comparison, the profiles of dimensionless current height $h^*(x^*)$ at $t^* = 2, 5, 6.5, 8, 9$ and 10.5 are shown in Figs. 7 and 8, respectively. These profiles are also defined at each time instant using the threshold value $\rho^* = 0.5$ [19–20]. The shape of the current at the initial acceleration phase $t^* = 2$ is similar for both tests S1 and S3. The
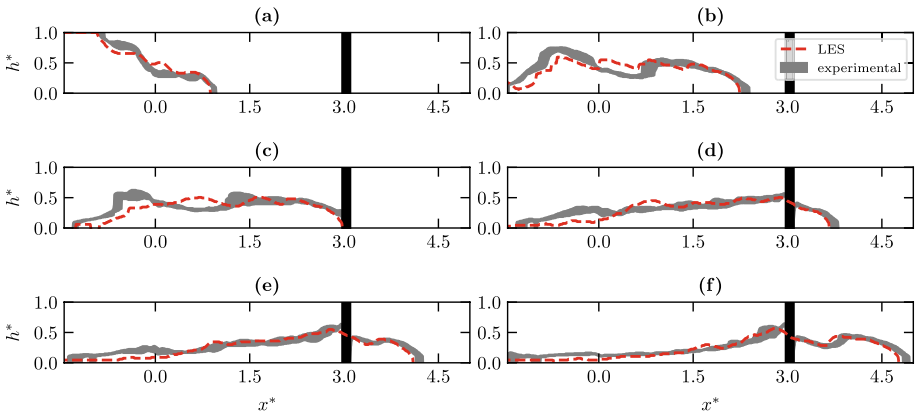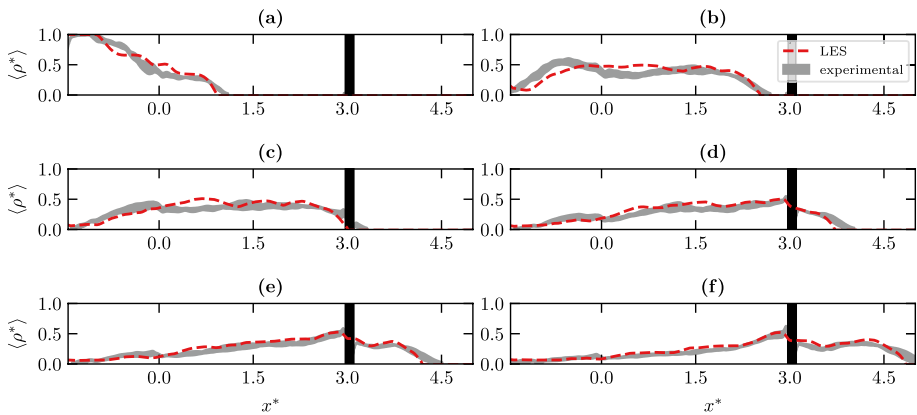
Fig. 8 LES (dashed red line) and experimental (shaded region) profiles of dimensionless current height h^* as a function of x^* for test S3 at **a** $t^* = 2$, **b** $t^* = 5$, **c** $t^* = 6.5$, **d** $t^* = 8$, **e** $t^* = 9$, and **f** $t^* = 10.5$
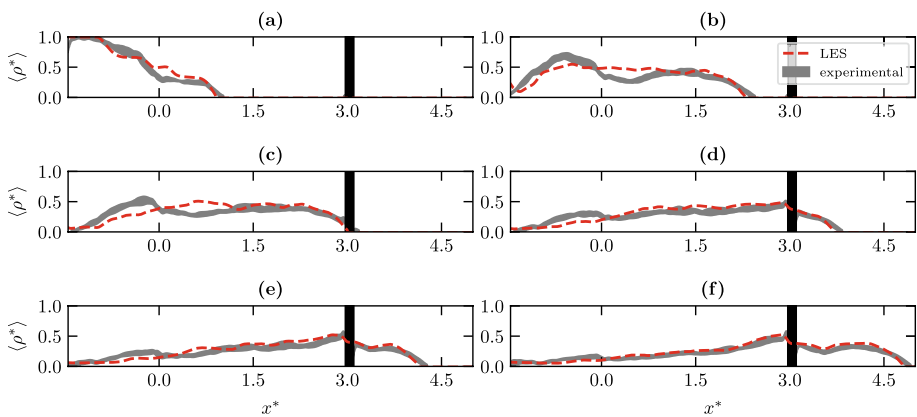

Fig. 9 LES (dashed red line) and experimental (shaded region) vertical profile of ρ^* for test S1 at $t^* = 10.5$ in the dimensionless position **a** $x^* = 1.5$, **b** $x^* = 2.5$, **c** $x^* = 3.5$ and **d** $x^* = 4.5$
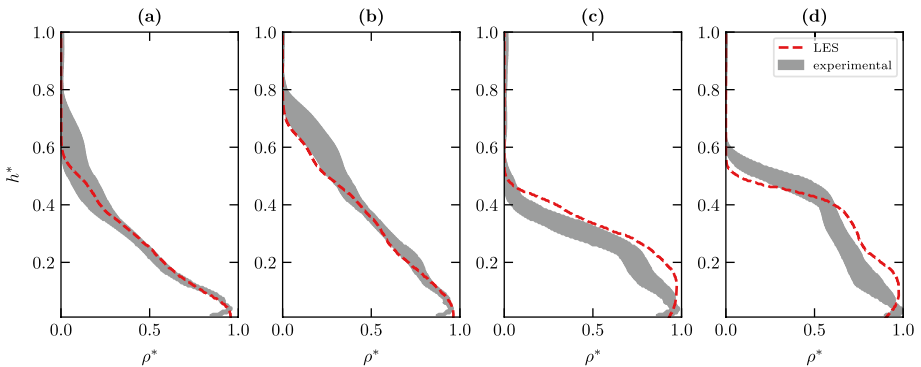
Fig. 10 LES (dashed red line) and experimental (shaded region) vertical profile of ρ^* for test S3 at $t^* = 10.5$ in the dimensionless position **a** $x^* = 1.5$, **b** $x^* = 2.5$, **c** $x^* = 3.5$ and **d** $x^* = 4.5$

Fig. 11 LES (dashed red line) and experimental (shaded region) profiles of dimensionless spanwise- and depth-averaged concentration $\langle \rho^* \rangle$ as a function of dimensionless position x^* for test S1 at **a** $t^* = 2$, **b** $t^* = 5$, **c** $t^* = 6.5$, **d** $t^* = 8$, **e** $t^* = 9$, and **f** $t^* = 10.5$

Fig. 12 LES (dashed red line) and experimental (shaded region) profiles of dimensionless spanwise- and depth-averaged concentration $\langle \rho^* \rangle$ as a function of dimensionless position x^* for test S3 at **a** $t^* = 2$, **b** $t^* = 5$, **c** $t^* = 6.5$, **d** $t^* = 8$, **e** $t^* = 9$, and **f** $t^* = 10.5$

average relative errors over the h^*–x^* plot is about 10%. After the collapse of the tail, there are some discrepancies, attributed to the different boundary conditions on the gate, including vaseline used in the experiments to prevent leakage. As the current advances, mainly during the impact of the current on the cylinder ($t^* > 6.5$), $h^*(x^*)$ upstream and downstream of the cylinder is well-defined, including the current surging and plunging. This good prediction of the current shape is independent of the g'_0. It can be seen in Figs. 7c–f and 8c–f that the LES collapse extremely well for $x^* > 1.5$, with average relative error less less than 5% even with slightly lower values of x^*_f (Fig. 3).

Figures 9 and 10 provide the vertical profiles of $\rho^*(h^*)$ at $t^* = 10.5$ in the position $x^* = 1.5, 2.5, 3.5$ and 4.5 for tests S1 and S3, respectively. The standard uncertainties associated with these features are larger than observed from current front position, of about 10%. Generally, along the h^* the shape of ρ^* predicted by the LES approach is closest to the

experiment measurements in almost all position, with average relative error less than 10%. The maximum difference between LES and experimental profiles at $t^* = 10.5$ occurs in $x^* = 3.5$ and $x^* = 4.5$ due to the flow plunging downstream $3 \lesssim x^* \lesssim 3.5$, current regrouping and the formation of a new head downstream of the cylinder (see Figs. 5–8). This strong unsteady 3D structure of the flow induces a large variation of the profiles with position. Thus, due to the small delay between LES and experimental position of the current (Fig. 3), the profiles can be very different.

The LES and experimental results of the dimensionless spanwise- and depth-averaged concentration $\langle \rho^* \rangle$ profiles are shown in Figs. 11 and 12. The main trends of $\langle \rho^* \rangle$ are well predicted with an average relative errors over the $\langle \rho^* \rangle$–x^* plot of about 10%. As the finite time upward lifting the gate is different from sudden removal some discrepancies on $\langle \rho^* \rangle$ occurs at $t^* = 2$. The trapped denser fluid in the lock region $x^* < 0$ and small dumping downstream of the current head for $0 < x^* < 1$ caused by the increasing of the resistance due to the vaseline can be confirmed in Figs. 11b–c and 12b–c. When the tail of the current leaves the lock region, similar $\langle \rho^* \rangle$ profiles are obtained for both tests S1 and S3, including the increasing of $\langle \rho^* \rangle$ upstream of the cylinder.

The LES and experimental evolution of the bulk entrainment coefficient E for tests S1 and S3 are compared in Fig. 13. In this paper, E is described by the time-variation of the side area of the density current as $E(t) = [\mathcal{S}(t) - \mathcal{S}_0]/\mathcal{S}_0$ [29], where $\mathcal{S}$ is the instantaneous side area of the density current in each time instant and $\mathcal{S}_0 = 1.5h_0^2$ is the initial side area of the lock (see, Fig. 1a). $\mathcal{S}(t)$ is calculated as

$$\mathcal{S}(t) = \int_0^{15h_0} \int_0^{h_0} \mathcal{W}(x, z, t) dz dx \qquad (9)$$

where $\mathcal{W}$ is a kernel function ($\mathcal{W} = 1$ if $\rho^* \geq 0.02$ and $\mathcal{W} = 0$ if $\rho^* < 0.02$). This threshold is usually adopted to isolate the instantaneous current body from ambient fluid and to calculate current interface with a high space-time resolution [1].

For test S1, the general shape of the entrainment E is reasonably predicted, except $t^* < 4$. This means that the entrainment is not fully reproduced by LES for the chosen ρ^* threshold. After the start of the impact ($t^* \gtrsim 6.5$), E becomes similar to the experimental, with a small relative error in the slope of about 5%. For test S3 (Fig. 13b), E is well predicted, with similar average slope over t^*. In fact, LES is within the uncertainties of the experiments for $t^* > 2$. However, LES lightly underpredicts E only for $t^* < 2$ due to the short initial acceleration phase. These discrepancies can be attributed to the large initial
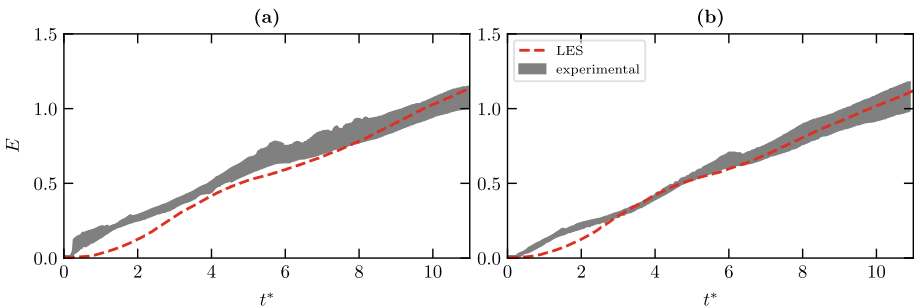

Fig. 13 LES (dashed red line) and experimental (shaded region) entrainment E as a function of t^* for tests **a** S1 and **b** S3

disturbance in the lifting of the gate and the distribution of mass, particularly for the smallest ρ^*.

4.3 Depth-averaged current structure

The depth-averaged dimensionless concentration contours $\rho^*(x^*, y^*, z_A^*, t^*)$ at four different dimensionless times $t^* = 6.5, 8, 9$ and 10.5 for tests P1 and P3 are compared in Figs. 14 and 15, respectively. As the cylinder wake flow is smoothed by the ensemble-averaging, LES contours in plan view are compared with a single experimental run. All tests show a good agreement between the LES and experimental contours. When the current arrives the cylinder at $t^* = 6.5$, the front structure shows similar streamwise ($x-$direction) gradient of ρ^*. At $t^* = 8$ a small detached volume of denser fluid in the current head is advected to the center of the channel ($y^* \approx 0$ and $x^* \approx 3.5$). This ungrouping of the current front is maintained by an envisaged unsteady 3D structure of the flow. This structure also traps a large amount of ambient fluid downstream of the cylinder $3 \lesssim x^* \lesssim 3.5$. Upstream of the cylinder there is an obstacle-induced increase of ρ^*. This effect promotes a large spanwise ($y-$direction) gradient of ρ^*, with maximum in the center and minimum close to lateral wall of the channel. After the head has passed the cylinder at $t^* = 9$, a small amount of ambient fluid remains trapped downstream of the cylinder but attached to it due to the backflow. This effect is not visible on the instantaneous spanwise-averaged concentration contours (side view tests) since the increase of the concentration on the lateral side of the cylinder compensates the lower density of the entrapped ambient fluid. At $t^* = 10.5$ a remarkable agreement of current regrouping and the formation of a new head downstream of the cylinder
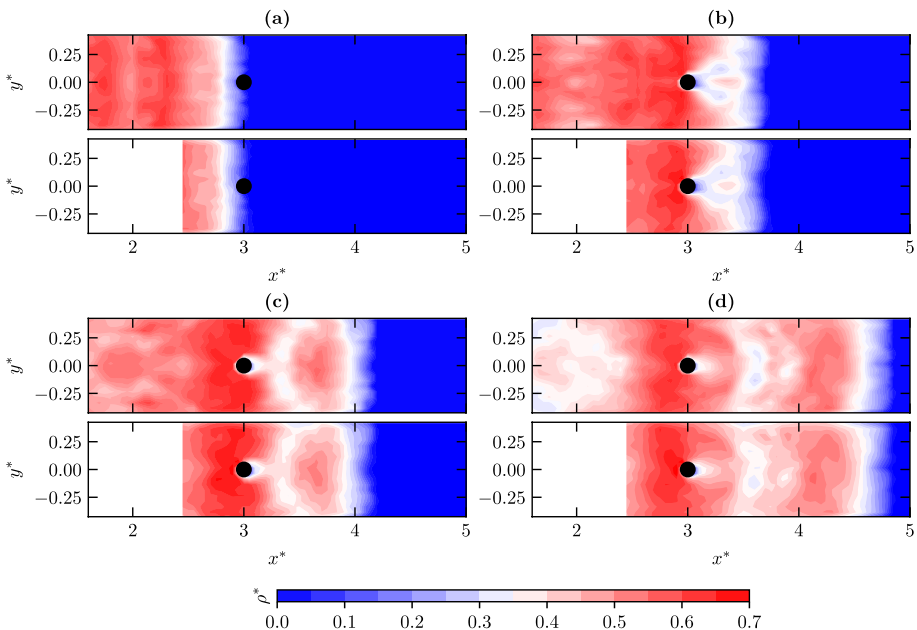
Fig. 14 LES (top) and experimental (bottom) instantaneous depth-averaged dimensionless concentration contours $\rho^*(x^*, y^*, z_A^*)$ for test P1 at **a** $t^* = 6.5$, **b** $t^* = 8$, **c** $t^* = 9$, and **d** $t^* = 10.5$
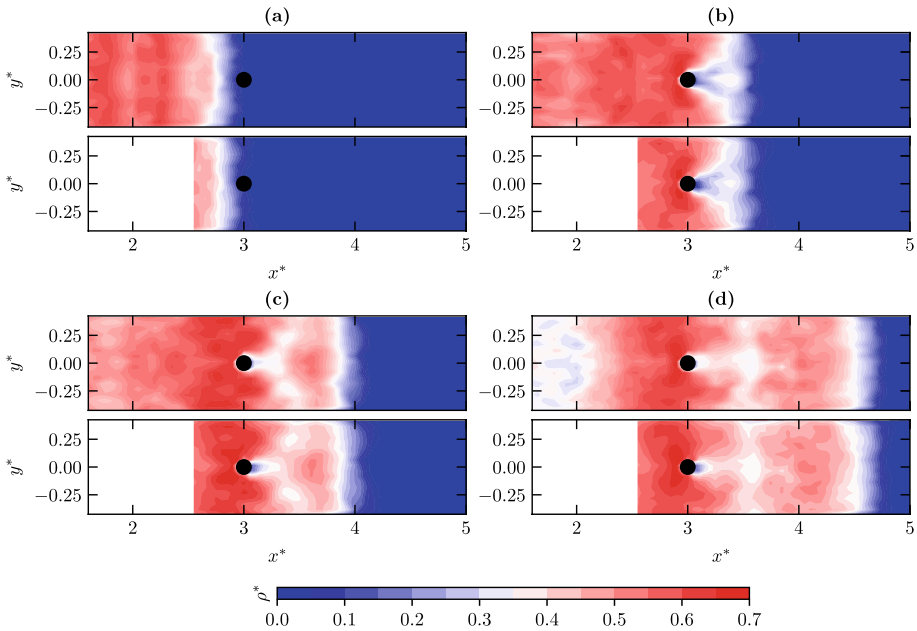
Fig. 15 LES (top) and experimental (bottom) instantaneous dimensionless depth-averaged concentration contours $\rho^*(x^*, y^*, z_A^*)$ for test P3 at **a** $t^* = 6.5$, **b** $t^* = 8$, **c** $t^* = 9$ and **d** $t^* = 10.5$

$3.5 \lesssim x^* \lesssim 4.5$ are found. The rear of the current head that occurs at $x^* \approx 3.5$ (Figs. 14c–d, and 15c–d) and the instabilities due to the unsteady vortex shedding and plunging of the current that changes the ρ^* are very well predicted.

4.4 Velocity field

Large eddy simulation and experimental velocity vector fields and profiles are compared and discussed through this section.

### 4.4.1 Velocity field upstream of the cylinder (side view)

Figures 16 and 17 provide detailed information of the dimensionless instantaneous velocity fields in the side view at the middle of channel $u^*(x^*, 0, z^*, t^*)$ and $w^*(x^*, 0, z^*, t^*)$ during the impact of the current on the cylinder for tests S1 and S3, respectively. As some billows in different runs are mismatched due to unsteady behavior and smoothed by the ensemble-averaged, only a single experimental run is presented. When the current front reaches the cylinder, at $t^* \approx 6.5$, a strong vertical velocity component is observed close to the current nose, caused by cylinder blocking effect. A billow structure at the interface of the two fluids in the rear of the current head occur almost same position $x^* \approx 2$. As the head passes the cylinder, the obstacle induces further billows at the interface and changes flow direction in the ambient fluid for $y^* \gtrsim 0.5$. This backflow is advected upwards ($z^* \gtrsim 0.75$) by the approach of rear of the current head at $t^* = 8$. This upper layer consists of an intermediate-density mixed fluid that results from the mixing between the ambient and source fluids
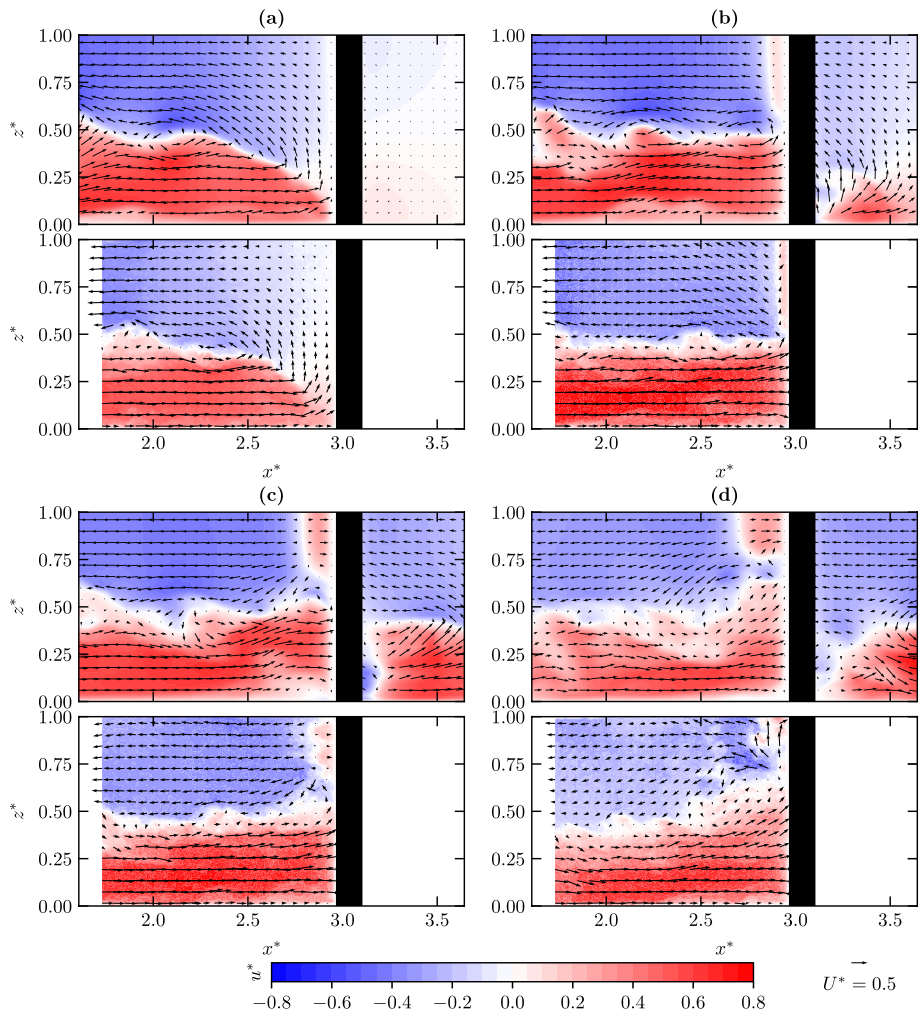
Fig. 16 LES (top) and experimental (bottom) instantaneous velocity field for test S1 at **a** $t^* = 6.5$, **b** $t^* = 8$, **c** $t^* = 9$, and **d** $t^* = 10.5$

within the head. Above the current there is a more diffuse region which is caused by the adverse pressure gradient. When the rear of the current head passes the cylinder a shock propagated upstream over the current is formed above the interface. This behavior is similar in all tests.

In order to further investigate the local feature of the velocity field, the vertical profiles of dimensionless horizontal component of the velocity field u^* are compared in Figs. 18 and 19 for tests S1 and S3, respectively. These profiles confirm that the LES results are in good match with the experimental data, most of the profiles perfectly collapse. However, near to the bottom of the channel for test S1 at $t^* = 8$ and 9 there are some differences, with maximum relative error of about 10%, caused by higher raised head in LES. This effect may be due to the Smagorinsky constant used, which depends on the flow characteristics close to the bottom.
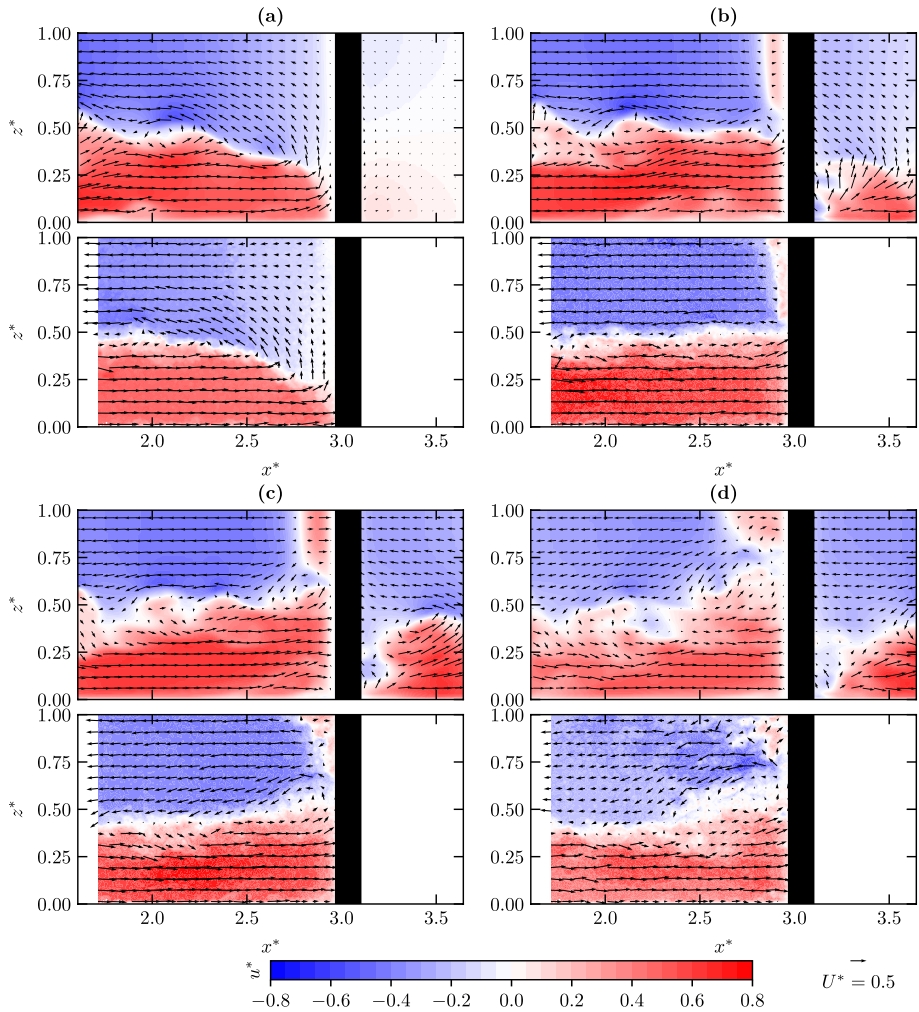
Fig. 17 LES (top) and experimental (bottom) instantaneous velocity field for test S3 at **a** $t^* = 6.5$, **b** $t^* = 8$, **c** $t^* = 9$, and **d** $t^* = 10.5$

Figure 20 compares the temporal evolution of depth-averaged $\langle u^* \rangle$ in the position $x^* = 2.5$. The LES and experimental evolution of $\langle u^* \rangle$ are calculated within the current body for $\rho^* \leq 0.5$. It can be observed that the shape of $\langle u^* \rangle$ predicted by the LES approach is very similar to the experiment measurements. In fact, in most of t^*, LES variation of $\langle u^* \rangle$ is within the experimental uncertainties. The standard uncertainty associated with $\langle u^* \rangle$ is of about 20%.

4.4.2 Velocity field in the wake of the cylinder (plan view)

Figures 21 and 22 provide detailed information of dimensionless instantaneous velocity fields in the plan view $u^*(x^*, y^*, 0.1, t^*)$ and $v^*(x^*, y^*, 0.1, t^*)$ during the impact of
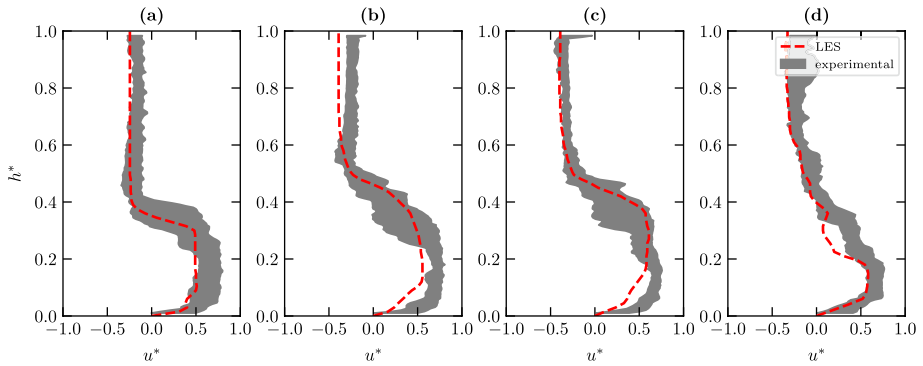
Fig. 18 LES (dashed red line) and experimental (shaded region) vertical profile of dimensionless stream-wise velocity u^* for test S1 in the position $x^* = 2.5$ at **a** $t^* = 6.5$, **b** $t^* = 8$, **c** $t^* = 9$ and **d** $t^* = 10.5$
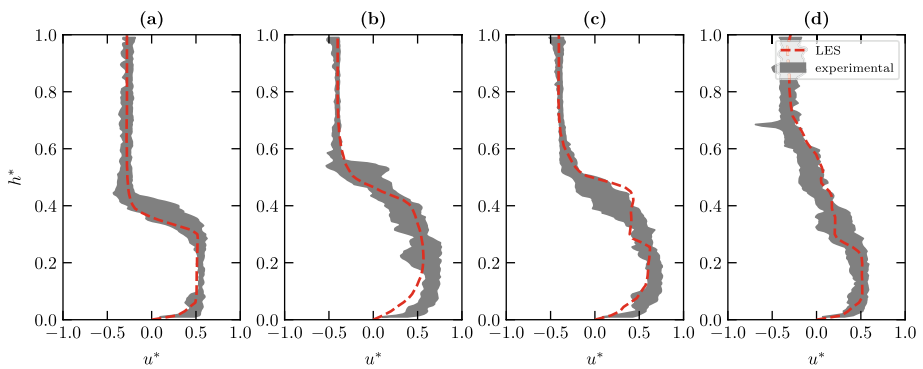
Fig. 19 LES (dashed red line) and experimental (shaded region) vertical profile of dimensionless stream-wise velocity u^* for test S3 in the position $x^* = 2.5$ at **a** $t^* = 6.5$, **b** $t^* = 8$, **c** $t^* = 9$ and **d** $t^* = 10.5$
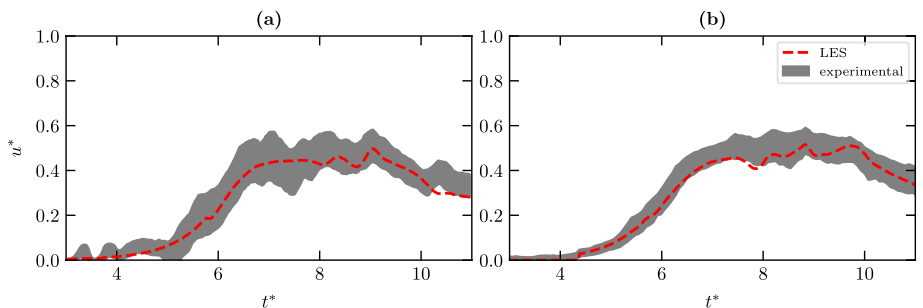

Fig. 20 Comparison of LES (dashed red line) and experimental (shaded region) temporal evolution of depth-averaged $\langle u^* \rangle$ within the current body for $\rho^* \leq 0.5$ in the position $x^* = 2.5$ for tests **a** S1 and **b** S3
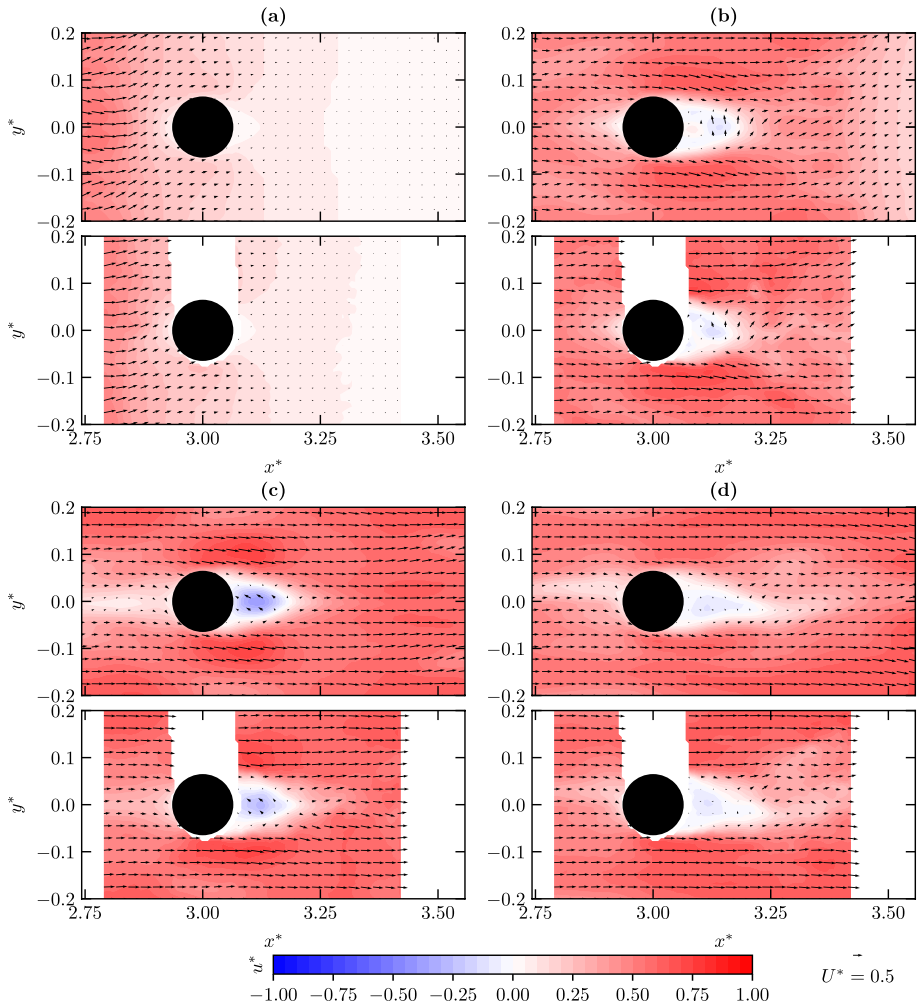
Fig. 21 LES (top) and experimental (bottom) instantaneous velocity field for test P1 at **a** $t^* = 6.5$, **b** $t^* = 8$, **c** $t^* = 9$, and **d** $t^* = 10.5$

the current on the cylinder for tests P1 and P3, respectively. When the current front reaches the cylinder $t^* \approx 6$, similar trends are observed in both tests. During this impact stage, the stagnation point occurs in the center of the cylinder ($y^* = 0$). As the head passes the cylinder, density current flows show several features with the well-studied constant-density flow past a circular cylinder. Here an unsteady wake structure is observed, with size depending on current head position. A strong similarities between LES solution and experimental measurements of the wake can be found in Figs. 21 and 22. The other tests conducted (not shown) within this investigation display similar behavior.
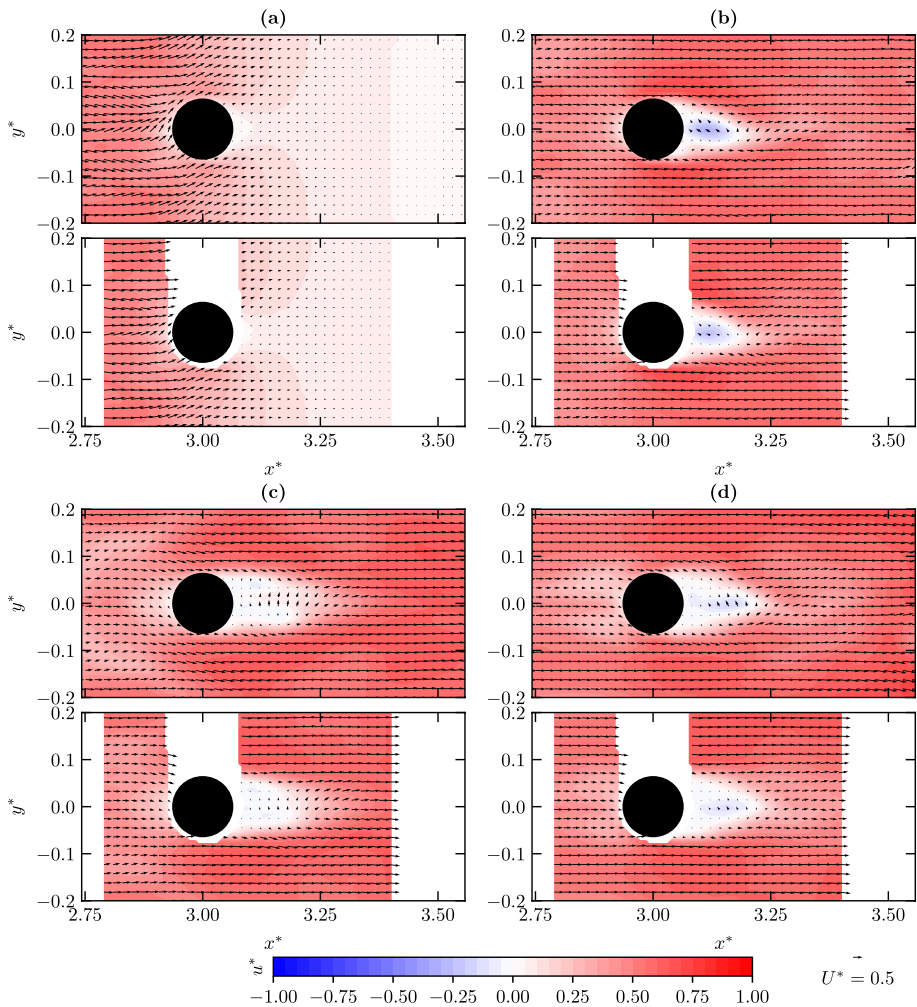
Fig. 22 LES (top) and experimental (bottom) instantaneous velocity field for test P3 at **a** $t^* = 6.5$, **b** $t^* = 8$, **c** $t^* = 9$, and **d** $t^* = 10.5$

5 Conclusions

This paper presents an extensive validation of large eddy simulation (LES) to predict the physics of lock-exchange density currents interacting with an emergent circular cylinder in the slumping phase. The validation was performed by comparing LES flow features with independent experimental data of both density and velocity fields. Measurements were performed in both side and plan views for cylinder Reynolds number range from 1300 to 3475. The qualitative and quantitative comparisons of LES solution and experimental measurements indicate that:

- A good agreement between LES and experimental kinematics of the current front was found for all values of the reduced gravity, with maximum relative error less than 8%. Clearly, the bulk current momentum is not affected by the cylinder, i.e., the slope of temporal evolution of the current front position is approximately constant. Large eddy simulation predicts slightly lower values of front position over the current propagation, however, with similar effective front speed.

- The main features of the time-space evolution of current spanwise- and depth-averaged density contours and instantaneous profiles of current height and concentration were also well predicted, showing the strength of LES to predict lock-exchange density currents interacting with bluff obstacles. The maximum difference between LES solution and experimental measurements occurs after the collapse of the tail, attributed to the different boundary conditions on the gate, including vaseline used in the experiments to prevent leakage. As the current advances, the effect of the gate on the current tail becomes negligible and the overall shape of the concentration contours were also quite similar. During the impact stage of the current on the cylinder, LES predicts the head nose slightly higher than the experimental, with a relative error of about 5%. However, the shape of the head remains approximately the same as the current advances. The obstacle-induced effect strongly modified the rear of the head with a surging of the current, i.e., an increasing of depth-average density, upstream of the cylinder. This current surging causes the plunging downstream after the head has passed the cylinder. The position of the wake and the shape of depth-averaged density profiles predicted by the LES were similar to the experiment measurements in almost all position, with average relative error less than 10%. The general shape of the bulk entrainment coefficient was well predicted, in most cases within the experimental uncertainties.

- Large eddy simulation time-space evolution of the current velocity fields in both side and top views are generally in excellent match with the experimental measurements. When the current front reaches the cylinder a strong local vertical velocity component was observed close to the current nose, caused by cylinder blocking effect. The billow structures at the interface of the two fluids in the rear of the current head occur almost in the same position. As the head passes the cylinder, the obstacle-induced promotes further billows at the interface and causes the flow surging upstream of the cylinder. This backflow is advected upwards by the approach of rear of the current head. A more diffuse region caused by the adverse pressure gradient was observed at the interface. When the rear of the current head passes the cylinder a shock propagated upstream over the current is formed above the interface, which was similar for all reduced gravity investigated. During this stage, similar trends of instantaneous velocity fields were observed downstream of the cylinder, specifically, in the size of wake structures. The vertical profiles of streamwise velocity confirm that the LES results are in excellent match with the experimental data, most of the profiles perfectly collapse. However, near to the bottom of the channel were found some differences, with maximum relative error of about 10%, caused by the raised head of the current. This effect may be due to the Smagorinsky constant used, which depends on the flow characteristics close to the bottom. Together, the temporal evolution of depth-averaged of streamwise component was within the experimental uncertainties.

All cases investigated in this paper demonstrated that the LES can be confidently used to describe the physics of flow-structure interaction in density currents. This validation was performed for simple layout that nonetheless pose challenges common to more complex systems. The next step is to investigate the turbulence characteristics of the flow in an array

of emergent cylinders, in order to provide an insight into the entrainment process and calibrate the diffusion terms.

References

1. Adduce C, Sciortino G, Proietti S (2012) Gravity currents produced by lock exchanges: experiments and simulations with a two-layer shallow-water model with entrainment. J Hydraul Eng 138:111–121
2. Bardoel SL, Horna Muñoz DV, Grachev AA, Krishnamurthy R, Chamorro LP, Fernando HJS (2021) Fog formation related to gravity currents interacting with coastal topography. Boundary-Layer Meteorol 181(2–3):499–521. https://doi.org/10.1007/s10546-021-00638-w
3. Bhaganagar K (2017) Role of head of turbulent 3-d density currents in mixing during slumping regime. Phys Fluids 29:020703
4. Bhaganagar K, Pillalamarri NR (2017) Lock-exchange release density currents over three-dimensional regular roughness elements. J Fluid Mech 832:793–824
5. Bombardelli FA, Cantero MI, Garcia MH, Buscaglia GC (2009) Numerical aspects of the simulation of discontinuous saline underflows: the lock-exchange problem. J Hydraul Res 47:777–789
6. Boussinesq J (1903) Theorie analytique de la chaleur, vol 2. Gauthier-Villars, Paris
7. Brito M, Sanches P, Ferreira RML, Covas DIC (2017) Experimental study of the transient flow in a coiled pipe using PIV. J Hydraul Eng 143:04016087
8. Cantero MI, Lee JR, Balachandar S, Garcia MH (2007) On the front velocity of gravity currents. J Fluid Mech 586:1–39
9. Cenedese C, Nokes R, Hyatt J (2016) Lock-exchange gravity currents over rough bottoms. Environ Fluid Mech 18:59–73
10. Cenedese C, Nokes R, Hyatt J (2018) Lock-exchange gravity currents over rough bottoms. Environ Fluid Mech 18:59–73
11. Constantinescu G (2013) LES of lock-exchange compositional gravity currents: a brief review of some recent results. Environ Fluid Mech 14:295–317
12. Daviero GJ, Roberts PJW, Maile K (2001) Refractive index matching in large-scale stratified experiments. Exp Fluids 31:119–126
13. Ermanyuk EV, Gavrilov NV (2005) Interaction of an internal gravity current with a submerged circular cylinder. J Appl Mech Tech Phys 46:216–223
14. Ermanyuk EV, Gavrilov NV (2005) Interaction of internal gravity current with an obstacle on the channel bottom. J Appl Mech Tech Phys 46:489–495
15. Farias R (2020) Caracterização experimental da interacção de correntes de densidade com um cilindro. Master's thesis MSc. Thesis, NOVA School of Science and Technology—FCT NOVA
16. Ferreira RM (2011) Turbulent flow hydrodynamics and sediment transport: laboratory research with lda and piv. In: Experimental methods in hydraulic research. Springer, pp 67–111
17. Fragoso AT, Patterson MD, Wettlaufer JS (2013) Mixing in gravity currents. J Fluid Mech 734
18. Gonzalez-Juez E, Meiburg E, Constantinescu G (2009) Gravity currents impinging on bottom-mounted square cylinders: flow fields and associated forces. J Fluid Mech 631:65–102
19. Gonzalez-Juez E, Meiburg E, Constantinescu G (2009) The interaction of a gravity current with a circular cylinder mounted above a wall: Effect of the gap size. J Fluids Struct 25:629–640
20. Gonzalez-Juez E, Meiburg E, Tokyay T, Constantinescuand G (2010) Gravity current flow past a circular cylinder: forces, wall shear stresses and implications for scour. J Fluid Mech 649:69–102
21. Hacker J, Linden P, Dalziel S (1996) Mixing in lock-release gravity currents. Dyn Atmos Oceans 24:183–195
22. Huppert HE, Simpson JE (1980) The slumping of gravity currents. J Fluid Mech 99:785–799
23. Issa R (1986) Solution of the implicitly discretised fluid flow equations by operator-splitting 62:40–65
24. Lollo GD (2021) Gravity currents interacting with an emergent obstacle. Master's thesis MSc. Thesis, Università Roma Tre
25. Mahdinia M, Firoozabadi B, Farshchi M, Varnamkhasti AG, Afshin H (2012) Large eddy simulation of lock-exchange flow in a curved channel. J Hydraul Eng 138:57–70

26. Mariono BM, Thomas LP, Linden PF (2005) The front condition for gravity currents. J Fluid Mech 536:49–78
27. Meiburg E, Radhakrishnan S, Nasr-Azadani M (2015) Modeling gravity and turbidity currents: computational approaches and challenges. Appl Mech Rev 67
28. Ooi SK, Constantinescu G, Weber L (2007) A numerical study of intrusive compositional gravity currents. Phys Fluids 19:076602
29. Ottolenghi L, Adduce C, Inghilesi R, Armenio V, Roman F (2016) Entrainment and mixing in unsteady gravity currents. J Hydraul Res 54:541–557
30. Ozan AY, Constantinescu G, Hogg AJ (2015) Lock-exchange gravity currents propagating in a channel containing an array of obstacles. J Fluid Mech 765:544–575
31. Pelmard J, Norris S, Friedrich H (2018) LES grid resolution requirements for the modelling of gravity currents. Comput Fluids 174:256–270
32. Pereira FS, Eça L, Vaz G, Girimaji SS (2021) Toward predictive RANS and SRS computations of turbulent external flows of practical interest 28:3953–4029
33. Ramos JP (2021) Experimental characterization of liquid-liquid stratified flow interacting with vertical emergent cylinders. Master's thesis MSc. Thesis, NOVA School of Science and Technology—FCT NOVA
34. Ricardo AM, Koll K, Franca MJ, Schleiss AJ, Ferreira RM (2014) The terms of turbulent kinetic energy budget within random arrays of emergent cylinders. Water Resour Res 50:4131–4148
35. Rocca ML, Adduce C, Sciortino G, Pinzon AB (2008) Experimental and numerical simulation of three-dimensional gravity currents on smooth and rough bottom. Phys Fluids 20:106603
36. Sher D, Woods AW (2015) Gravity currents: entrainment, stratification and self-similarity. J Fluid Mech 784:130–162
37. Simpson JE (1997) Gravity currents in the environment and the laboratory. Cambridge University Press
38. Smagorinsky J (1963) General circulation experiments with the primitive equations i. The basic experiment. Mon Weather Rev 91:99–164
39. Solis GN (2018) Gravity currents propagating over and within a porous bed. Master's thesis MSc. Thesis, Università Roma Tre
40. Tokyay T, Constantinescu G, Gonzalez-Juez E, Meiburg E (2011) Gravity currents propagating over periodic arrays of blunt obstacles: effect of the obstacle size. J Fluids Struct 27:798–806
41. Tokyay T, Constantinescu G, Meiburg E (2012) Tail structure and bed friction velocity distribution of gravity currents propagating over an array of obstacles. J Fluid Mech 694:252–291
42. van Leer B (1979) Towards the ultimate conservative difference scheme. v. a second-order sequel to godunov's method 32:101–136
43. van Sommeren DDJA, Caulfield CP, Woods AW (2012) Turbulent buoyant convection from a maintained source of buoyancy in a narrow vertical tank. J Fluid Mech 701:278–303
44. Zhou J, Cenedese C, Williams T, Ball M, Venayagamoorthy SK, Nokes RI (2017) On the propagation of gravity currents over and through a submerged array of circular cylinders. J Fluid Mech 831:394–417